Applied Catalysis B: Environmental 210 (2017) 121–130

Contents lists available at ScienceDirect

Applied Catalysis B: Environmental

journal homepage: www.elsevier.com/locate/apcatb

Research paper

Carbon nanotube supported PdAg nanoparticles for electrocatalytic oxidation of glycerol in anion exchange membrane fuel cells

Neeva Benipal[a], Ji Qi[a,1], Qi Liu[a], Wenzhen Li[a,b,*]

[a] Department of Chemical and Biological Engineering, Biorenewables Research Laboratory, Iowa State University, Ames, IA, 50011, USA
[b] Ames Laboratory, US-DOE, Ames, IA, 50011, USA

ARTICLE INFO

Article history:
Received 1 December 2016
Received in revised form 27 February 2017
Accepted 28 February 2017
Available online 10 March 2017

Keywords:
Biomass renewables
Glycerol oxidation
Anion-exchange membrane fuel cell
PdAg nanoparticles
Electrocatalysis

ABSTRACT

Electro-oxidation of alcohol is the key reaction occurring at the anode of a direct alcohol fuel cell (DAFC), in which both reaction kinetics (rate) and selectivity (to deep oxidation products) need improvement to obtain higher power density and fuel utilization for a more efficient DAFC. We recently found that a PdAg bimetallic nanoparticle catalyst is more efficient than Pd for alcohol oxidation: Pd can facilitate deprotonation of alcohol in a base electrolyte, while Ag can promote intermediate aldehyde oxidation and cleavage of C—C bond of C_3 species to C_2 species. Therefore, a combination of the two active sites (Pd and Ag) with two different functions, can simultaneously improve the reaction rates and deeper oxidation products of alcohols (Applied Catalysis B, 2016, 199, 494). In this continuing work, Pd, Ag mono, and bimetallic nanoparticles supported on carbon nanotubes (Ag/CNT, Pd/CNT, Pd_1Ag_1/CNT, and Pd_1Ag_3/CNT) were prepared using an aqueous-phase reduction method; they served as working catalysts for studying electrocatalytic oxidation of glycerol in an anion-exchange membrane-based direct glycerol fuel cell. Combined XRD, TEM, and HAADF-STEM analyses performed to fully characterize as-prepared catalysts suggested that they have small particle sizes: 2.0 nm for Pd/CNT, 2.3 nm for PdAg/CNT, 2.4 nm for $PdAg_3$/CNT, and 13.9 nm for Ag/CNT. XPS further shows that alloying with Ag results in more metal state Pd presented on the surface, and this may be related to their higher direct glycerol fuel cell (DGFC) performances. Single DGFC performance and product analysis results show that PdAg bimetallic nanoparticles can not only improve the glycerol reaction rate so that higher power output can be achieved, but also facilitate deep oxidation of glycerol so that a higher faradaic efficiency and fuel utilization can be achieved along with optimal reaction conditions (increased base-to-fuel ratio). Half-cell electrocatalytic activity measurement and single fuel cell product analysis of different glycerol oxidation intermediates, including C_3: glycerate, tartronate, mesoxalate, and lactate; C_2: glycolate and oxalate, over PdAg/CNT catalyst was further conducted and produced deeper insight into the synergistic effects and reaction pathways of bimetallic PdAg catalysts in glycerol electrocatalytic oxidation.

1. Introduction

Rapid depletion of fossil fuels makes it necessary to seek replacement of petroleum-based energy sources to lead to a sustainable future [1]. Clean and renewable energy sources are increasingly being used to replace fossil fuels, to end the progression of climate change, and to reduce pollution [2]. Prominent energy devices such as internal combustion engines have low efficiency (<13%) while emitting many harmful pollutants and greenhouse gasses [3]. Glycerol is a non-toxic, non-flammable, and non-volatile biorenewable alcohol fuel obtained as a byproduct of the transesterification reaction that occurs in the production of biodiesel [4–6]; as a result, glycerol can today be obtained at relatively lower market prices compared to other alcohol fuels (see Table 1). Glycerol can serve as a starting point for production of a series of high-value oxygenated chemicals such as glyceric acid, tartronic acid, mesoxalic acid, and glycolic acid, etc. [7–11]. Traditional production of these oxygenate compounds is costly, environmentally unfriendly because of stoichiometric oxidation using strong acids [12], or exhibits slow fermentation processes accompanied by low output yields [13]. A glycerol oxidation reaction (GOR) produces negative Gibbs free energy, so it can be used as a fuel fed at the anode for fuel cells

* Corresponding author at: Department of Chemical and Biological Engineering, Biorenewables Research Laboratory, Iowa State University, Ames, IA, 50011, USA.
E-mail addresses: liwenzhen@gmail.com, wzli@iastate.edu (W. Li).
[1] Current address: School of Chemical Engineering, Dalian University of Technology, Dalian 116023, China.

http://dx.doi.org/10.1016/j.apcatb.2017.02.082
0926-3373/

Table 1
The state-of-the-art of oxygen-based direct alcohol fuel cells.

Fuel	Fuel cost (US$/gallon)	Catalyst cost (mg_{Pt}/cm^2 MEA)	AMFC (mW/cm^2)	PEMFC (mW/cm^2)	SOFC (mW/cm^2)
Crude glycerol	0.75–0.9	0.5	269[a] [25]	–	–
Refined glycerol	4.0–4.8	0.5	285[a] [25]	–	327[b] [26]
Methanol	1.3	>10	168 [27]	246 [28]	1600[b] [29]
Ethanol	3.2	>5	185 [30]	80 [31]	800[b] [32]

[a] Li group previous results.
[b] >750 °C operation. AM: alkaline membrane, PEM: proton exchange membrane, SO: solid oxide, FC: fuel cell, MEA: membrane electrode assembly.

to simultaneously generate electrical power and produce valuable chemicals.

Fuel cells, batteries, and electrochemical capacitors are systems considered for alternative energy/power sources. The main disadvantage of rechargeable batteries (mostly lithium-based, e.g., lithium or lithium polymer) is limited energy density [14,15]. Fuel cell technology, a thrust research area, is an appropriate substitute to rechargeable battery technology due because fuel cells, especially direct alcohol fuel cells (DAFCs), have been recognized as green energy generators capable of converting renewable sources into electrical power [16]. To meet the world's demand for energy, DAFCs represent a potentially promising alternative energy source to the use of fossil fuels [17,18]. The thermodynamic efficiency of a DAFC is greater than 90% because energy from the fuel is directly transformed into electrical energy without the constraints of Carnot's theorem [19,20]. Anion-exchange membrane-direct alcohol fuel cells (AEM-DAFCs) have the great advantage that the kinetics of both anode and cathode reactions can be greatly enhanced by the better mass transfer and lower adsorption of spectator-charged species [17,18,21–24]. The byproducts associated from AEM-DAFCs also appear to produce no negative environmental impact. To more completely explore such alternative fuels, numerous studies have been carried out based on AEMFC platforms using various biorenewable fuels.

The typical performances of DAFCs are shown in Table 1. Low-temperature AMFCs have exhibited significant advantages over other types of fuel cells because charge and ion transfer along with alcohol oxidation kinetics can be greatly improved in alkaline media. We have demonstrated a surprisingly high performance of 268.5 mW/cm^2 (ambient O_2, with a low Pt loading of 0.5 mg/cm^2, 80°C) using an AEMFC directly fed with 88 wt% soybean biodiesel crude glycerol (one of the cheapest alcohols on the market), with the faradaic efficiency reaching 47% ($6.5e^-/14e^-$) [25]. In general, a PEM-direct ethanol fuel cell has a peak power density (e.g., <80 mW/cm^2) and low faradaic efficiency of <30% because its dominant byproduct is acetate (4e/12e). SOFCs must operate at high temperatures (i.e. >750°C) and thus have relatively limited applications for portable electronics. Current biofuel cells employ enzymatic catalysts to achieve complete oxidation of alcohols, but their low output power density (<1.0 mW/cm^2), heavy dependence on the organic-living environment, and short lifetime limit biofuel cell applications to environmental remediation rather than mobile power source application. To achieve long life-time DGFCs operation, however, more robust and cheaper catalysts must be developed.

Platinum (Pt) and Pt-based catalysts for DAFCs have been identified as the best electro-catalysts with respect to electrooxidation of alcohols at relatively low temperatures, where they exhibited high power density and fuel utilization efficiency [25,33–37]. Pt can be more easily contaminated than other precious metals, limiting its stability and activity, and the high cost due to scarcity of Pt is also problematic, so extensive efforts are being carried out to rationally design new catalysts for DAFCs. Much research regarding selective oxidation of glycerol through environmentally-friendly and fast heterogeneous catalysis using monometallic/bimetallic Pd based catalysts has been conducted [7,12,38–41]. Since Pd is much more abundant in nature and half the cost of Pt, it is a suitable replacement of Pt for oxidation of a large variety of organic molecules in alkaline environments. The addition of a second metal to create Pd-M alloy catalysts has been extensively explored [42–50]. For a C_{2+} alcohol, there is a need to rationally design Pd-M catalysts to not only improve the oxidation kinetics (activity), but also to manipulate the reaction pathway to cleave a C—C bond of alcohol. Ag has up to now been much less studied in heterogeneous oxidation catalysis, even though its addition to Pd can significantly reduce the cost of the anode catalyst and may even further improve the alcohol oxidation rate. We recently designed an efficient PdAg/CNT catalyst that demonstrated better performance than Pd/CNT for alcohol (methanol, ethanol, ethylene glycol, and glycerol) oxidation in AEM-DAFCs [51]. We found that Pd can facilitate deprotonation of alcohol in a base electrolyte, while Ag can promote intermediate aldehyde oxidation and cleavage of C—C bonds of C_3 species to C_2 species, so a combination of two active sites (Pd and Ag), with two different functions, can simultaneously improve both the reaction rate and the deeper oxidation products. Previous work focused on the PdAg/CNT catalyzed alcohol oxidation reaction facilitated by Ag catalyzed aldehyde oxidation, a more general catalytic mechanism.

In the present work, we focus on a more detailed analysis of glycerol oxidation over PdAg/CNT as well as a more comprehensive physical characterization of PdAg/CNT. Full characterizations such as XRD, TEM, XPS, ICP-MS, and HAADF-STEM, were used to characterize the particle size, size distribution, structure, surface chemical state and bulk metal composition of these catalysts. The catalytic activities of catalysts toward glycerol oxidation were first compared in half-cells, and then applied as electrocatalysts for oxidation of glycerol in AEM-DAFCs to determine the product distribution. Electrocatalytic activities of different reaction intermediates (C_3 chemicals: glycerate, tartronate, mesoxalate, lactate; C_2 chemicals: glycolate, oxalate) corresponding to these catalysts were determined to investigate the reaction pathways, with combined product distribution results obtained in single DGFCs. This study demonstrates the benefit of using an alloyed Pd-Ag bimetallic catalyst to improve peak power density and facilitate deeper oxidation products, thereby improving fuel cell performance.

2. Experimental

2.1. Chemicals

Carboxyl-group functionalized short multi-wall carbon nanotubes (8–15 nm outer diameter, 0.5–2 mm length) were purchased from Cheaptubes, Inc. Palladium (II) nitrate dihydrate (40%), silver nitrate (99%), 1-propanol (99.5%), potassium hydroxide (85%), potassium sulfate (99%), sodium borohydride (99%), sodium citrate dihydrate (99%), polytetrafluoroethylene (PTFE) ionomer solution (60%), glycerol (99.5%), lactic acid (98%), D-glyceric acid calcium salt dihydrate (99%), sodium mesoxalate monohydrate (98%), tartronic acid (97%), glycolic acid (99%), and oxalic acid (99%) were obtained from Sigma-Aldrich. The cathode Acta 4020 catalyst (Fe-based) was

bought from Acta, Inc. All chemicals were used as received without further purification.

2.2. Catalyst synthesis and physical characterizations

Carbon-nanotube (CNT) supported nanoparticles Pd/CNT, PdAg/CNT, $PdAg_3$/CNT, and Ag/CNT catalysts (20 wt%) were synthesized using a modified aqueous-phase reduction method recently developed by our group [25,51–53]. The prepared catalysts were characterized using transmission electron microscopy (TEM, JEOL 2010) with an operating voltage of 200 kV. X-ray diffraction (XRD) patterns were collected from a Scintag XDS-2000 *q/q* diffractometer using Cu *K*a radiation (l = 1.5406 Å), with a tube current of 35 mA and a tube voltage of 45 kV. The mean crystallite size of catalysts was calculated using the (220) peak based on a combination of Bragg's law and the relationship between lattice and crystal-lattice spacing given by

$$L = \frac{0.9\lambda_{K\alpha}}{B_{2\theta}\cos\theta_{\max}}$$

where L is the mean crystallite size, $\lambda_{K\alpha}$ is the X-ray wavelength (1.5406 Å), B is the full width of the peak (rad) at half-maximum (FWHM), and q_{max} is the Bragg angle (rad) of the (220) peak position. X-ray photoelectron spectroscopy (XPS) measurements were performed using a Kratos Amicus/ESCA 3400 with Mg Ka X-rays (1253.6 eV). During XPS analysis samples were not sputtered. All spectra were calibrated with a measured C 1s peak at 284.6 eV. High-angle annular dark field images were obtained using aberration-corrected scanning transmission electron microscopy (HAADF-STEM) on a Titan Themis electron microscope at 300 KV with a super-X EDS detector.

2.3. Electrocatalytic oxidation of glycerol and reaction intermediates in athree-electrode cell

Cyclic voltammetry was performed in a single compartment three-electrode setup (AFCELL3, Pine Instrument), consisting of a glassy carbon working electrode (AFE3T050GC, Pine Instrument), a coiled platinum counter electrode (AFCTR1, Pine Instrument) isolated by a fritted glass tube from the main test electrolyte, a Hg/HgO reference electrode (MMO, CHI152, CH Instruments), with a 0.1 M KOH filling solution. The potential was applied with a multi-channel potentiostat (Biological). The tests were prepared and performed at 25°C or 60°C temperature and all potentials in the study were referred to MMO (1.0 M KOH, 0.098 V vs. SHE). The prepared catalyst's ink was dispersed by ultrasonication in 1-propanol to form a uniform ink (0.5 mg mL^{-1}). A glassy carbon electrode (GCE) was refined with an alumina micropolish solution and grinding paper to avoid contamination by metal particles. The working electrode was prepared by drop-casting 10 mL of ink for Pd/CNT and Ag/CNT, 20 mL of ink for PdAg/CNT, and 40 mL of ink for $PdAg_3$/CNT with a micro-syringe onto a polished and cleaned GCE with a working area of 0.1963 cm^2. 10 mL of 0.05 wt% AS-4 anion conductive ionomer solution (Tokuyama, Inc) was added on top to affix and bind the catalyst particles. The electrolytes were composed of 1.0 M KOH + 0.1 M glycerol, mesoxalic acid, glyceric acid, tartronic acid, oxalic acid, lactic acid, or glycolic acid in deionized water. Prior to testing, all electrolytes were de-aerated by purging with high purity N_2 for 30 min at ambient temperature. Ten cyclic voltammograms (CVs) were recorded for each catalyst at a constant sweep rate of 50 mV^{-1} at 25°C or 60°C.

2.4. Electrocatalytic oxidation of glycerol in anion exchange membrane–direct glycerol fuel cells (AME-DGFCs)

The fuel cell tests were performed on a Scribner Fuel Cell System 850e (Scribner Associates, USA) using a self-constructed membrane electrode assembly (MEA), a serpentine graphite flow field plate, and a feedback temperature control loop composed of electric heating rods and a thermocouple thermometer. The membrane-electrode assembly (MEA), with an active area of 5 cm^2, consisted of a solid anion-exchange membrane (A901, 10 μm) mechanically sandwiched between anode and cathode catalyst layers on carbon cloth. Self-prepared Pd/CNT, PdAg/CNT, $PdAg_3$/CNT, and Ag/CNT served as anode catalysts, while commercial Acta 4020 was used as the cathode catalyst. The catalyst 4020 is Acta 4020 cathode catalyst, a noble-metal-free Fe-based cathode catalyst for use in alkaline membrane fuel cells. Standard composition of this catalyst is approx. 3.5% wt. transition metal (Fe-based) on carbon support. The anode catalyst ink was made by dispersing the anode catalyst powder and a 10 wt% PTEF solution (catalyst: PTFE = 8:2 mass ratio) in 1-propanol by ultra-sonication in an ice-water bath for 40 min to form a uniform ink dispersion (10 $mg_{catalyst}$ mL^{-1}) sprayed onto the carbon cloth with a spray gun. The mass of the catalyst on the carbon cloth was calculated as yielding a metal loading of 0.5 mg cm^{-2} for both Pd/CNT and Ag/CNT, 1.0 mg cm^{-2} for PdAg/CNT, and 2.0 mg cm^{-2} for $PdAg_3$/CNT. The cathode catalyst ink was prepared by blending the cathode catalyst powder and an AS-4 anion conductive ionomer (catalyst:AS-4 = 7:3) in 1-propanol by ultrasonication in an ice-water bath for 40 mins to form a homogenous ink dispersion that was directly sprayed on the AEM. The mass of catalyst on the AEM was calculated as providing a catalyst loading of 3.0 mg cm^{-2}. Additional details of fuel cell design can be found in our previous work [19,54,55]. The fuel was pumped through a peristaltic pump into the anode at a flow rate of 4.0 mL min^{-1} for performance tests and 1.0 mL min^{-1} for product analysis, while high-purity O_2 was fed into the cathode compartment at a flow rate of 0.2 L min^{-1} for performance tests and 0.1 L min^{-1} for product analysis at a backpressure of 0 psig.

2.5. Product analysis of glycerol oxidation in AEM-DGFC

20 mL of 4.0 M KOH + 1.0 M glycerol solution was cycled with a flow rate of 1.0 mL min^{-1} using a peristaltic pump between a plastic vessel and the anode chamber via a closed loop (Gilson Minipuls 3). High purity O_2 (>99.999%) was fed into the cathode compartment at a flow rate of 0.1 L min^{-1}. Electrocatalytic glycerol oxidation was performed at 60°C for 2 h at a constant voltage of 0.1 V. Product samples were periodically obtained throughout the test for analysis by high performance liquid chromatography unit (HPLC, Agilent 1100, Alltech OA-1000 column, 60°C) equipped with a refractive index detector (RID, Agilent G1362A), and a variable wavelength detector (VWD, Agilent G1314A, 220 nm). An eluent of 5 mM aqueous sulfuric acid at a flow rate of 0.3 mL min^{-1} was applied for product separation. 20 mL of sample was injected into the HPLC system. All product samples were identified by comparison with standard samples. Throughout this paper, all investigated products were in their deprotonated (salt) forms in alkaline media; but for convenience of comparison with previous studies, we have reported them in acid forms.

The product selectivity, glycerol conversion (Xg), carbon balance, and fuel utilization (ϵ_f) were calculated using the following equations:

$$S = \frac{\text{moles of } C_2 \text{or } C_3 \text{product}}{\text{total moles of } C_2 \text{and } C_3 \text{products}} \times 100\%$$

$$X_g = \left(1 - \frac{\text{residual moles of glycerol after reaction}}{\text{total moles of glycerol}}\right) \times 100\%$$

$$\text{Carbon balance} = \frac{\Sigma\left(M_{C_1} + M_{C_2} + M_{C_3}.....M_{C_f}\right)}{M} \times 100\%$$

$$\varepsilon_f = \varepsilon_e \times X_g$$

where S is the selectivity of one C_2 or C_3 reaction intermediates; Xg is the conversion of glycerol; M is the number of moles of glycerol in the electrolyte, M_C is the number of moles of carbon in each product, ε_f is fuel efficiency or fuel utilization, and ε_e is faraday efficiency [51].

3. Results and discussion

3.1. Physical characterization of monometallic and bimetallic Pd and Ag electrocatalysts

Carbon nanotube (CNT) supported monometallic Pd/CNT and Ag/CNT and bimetallic PdAg/CNT and $PdAg_3$/CNT were prepared using a modified aqueous-phase reduction method [51]. The morphology, particle size, size distribution, structure, surface chemical state, and composition of the as-prepared catalysts were analyzed by X-ray diffraction (XRD), transmission electron microscopy (TEM), high-angle annular dark field *via* aberration-corrected scanning transmission electron microscopy (HAADF-STEM), X-ray photoelectron spectroscopy (XPS), and inductively coupled-plasma- mass spectrometry (ICP-MS). XRD patterns of all catalysts, collected at temperature ranging from 15° to 90°, exhibited typical a face-centered cubic (FCC), as shown in Fig. 1a. The diffraction peaks that correspond to monometallic Pd are 40°, 47°, 68°, and 81° representing the (111), (200), (220), and (311) facets, respectively. For monometallic Ag, diffraction peaks are centered at 38°, 44°, 64°, 77°, and 82°, representing the (111), (200), (220), (311), and (222) facets, respectively. The diffraction peaks of the alloyed PdAg and $PdAg_3$ bimetallic nanoparticles fall between those of monometallic Ag and Pd, suggesting the formation of alloy structure. No obvious phase separation is observed for either PdAg/CNT or $PdAg_3$/CNT. It was also noted that the XRD diffraction peaks shifted to larger angles gradually with the increase of Ag content.

The mean crystalline sizes of Ag/CNT, $PdAg_3$/CNT, PdAg/CNT, and Pd/CNT catalysts, calculated based on their (220) diffraction peaks using the Debye-Scherrer formula, were 13.9, 2.4, 2.3, and 2.0 nm, respectively. The TEM images of Ag/CNT, $PdAg_3$/CNT, PdAg/CNT, and Pd/CNT and the corresponding metal particle size histograms are shown in Fig. 1b–e. The average particle sizes evaluated from the TEM were 13.7, 2.4, 2.3, and 2.1 nm for Ag/CNT, $PdAg_3$/CNT, PdAg/CNT, and Pd/CNT, respectively, in good agreement with the results from the XRD results. The histograms of particle sizes determined from 100 randomly chosen particles in arbitrary areas showed a narrow size distribution of 10.3–18.0 nm for Ag/CNT, 1.9–3.2 nm for $PdAg_3$/CNT, 1.6–2.9 nm for PdAg/CNT, and 1.4–2.8 nm for Pd/CNT. It can be observed that well-dispersed metal particles were uniformly deposited on the CNT support. The similar particle sizes and size distributions of these catalysts (Pd/CNT, PdAg/CNT, $PdAg_3$/CNT) provide a good platform for investigating selective electrooxidation of glycerol in alkaline electrolyte. The aqueous-phase reduction method achieved very small Pd nanoparticles under these synthesis conditions, while the Pd-Ag containing particles were slightly larger and more highly developed. Bulk metal compositions of monometallic and bimetallic catalysts were close to the set metal loading (20 wt%), indicating that Pd and Ag precursors were fully reduced during nanoparticle synthesis.

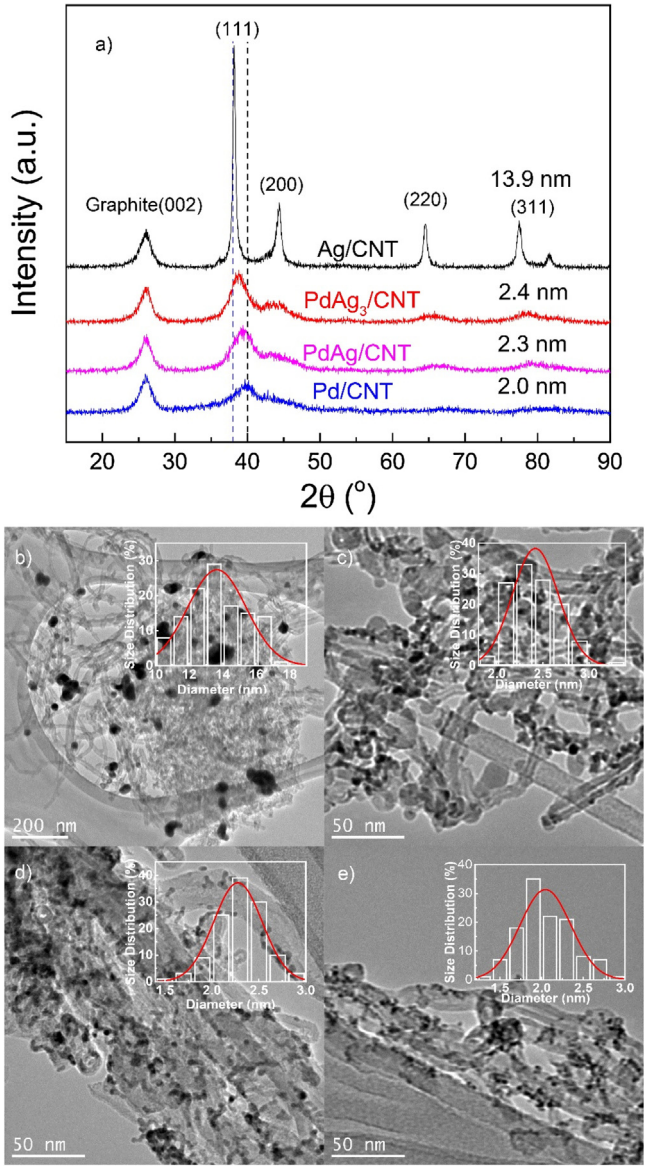

Fig. 1. XRD patterns of (a) Ag/CNT, $PdAg_3$/CNT, PdAg/CNT, and Pd/CNT catalysts. TEM images and corresponding particle size histograms of (b) Ag/CNT, (c) $PdAg_3$/CNT, (d) PdAg/CNT, and (e) Pd/CNT catalysts.

XPS was further used to characterize the surface oxidation states of the metals in as-prepared catalysts, and a survey XPS spectrum confirmed the coexistence of Pd, Ag, C, and O elements in as-prepared catalyst. The oxidation states of Pd and Ag were obtained by fitting the peaks of high resolution Pd 3d and Ag 3d XPS spectra, as shown in Fig. 2a and b. XPS spectra of monometallic Pd/CNT revealed both oxidized Pd^{2+} and metallic Pd^0 chemical oxidation states (Fig. 2a). The addition of Ag to Pd when alloyed prevents the oxidation of Pd, so in alloyed PdAg/CNT and $PdAg_3$/CNT the existence of only metallic Pd^0 in the surface oxidation state was observed. Metallic Ag^0 was primarily present in Ag 3d of Ag/CNT, PdAg/CNT, and $PdAg_3$/CNT catalysts, as shown in Fig. 2b. Pd^0, Pd^{2+}, and Ag^0 were detected, reflecting the efficient reduction of $Pd(NO_3)_2{\cdot}2H_2O$ and $AgNO_3$. A greater amount of metallic Pd^0 in PdAg/CNT catalyst may lead to a better alcohol deprotonation effect than for monometallic Pd/CNT, resulting in higher glycerol oxidation kinetics. The low intensity for Ag is due to larger particle size. Furthermore, XPS were performed on as-prepared catalysts after a 2 h reaction under hard conditions of alkaline electrolyte

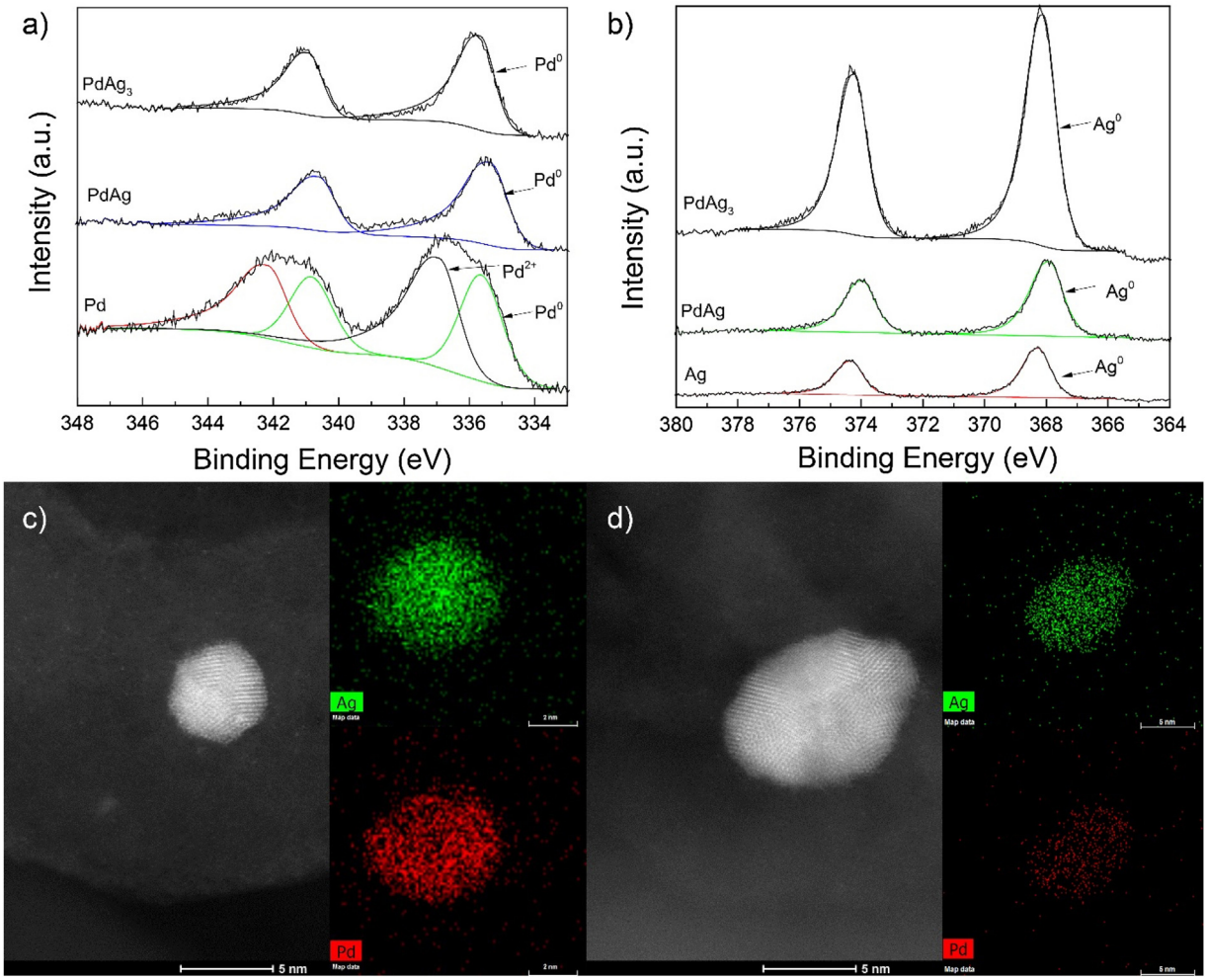

Fig. 2. XPS spectra of as-prepared catalysts before 2 h glycerol oxidation in AEMFC a) Pd 3d for Pd/CNT, PdAg/CNT, and $PdAg_3$/CNT, b) Ag 3d for Ag/CNT, PdAg/CNT and $PdAg_3$/CNT. HAADF-STEM-EDS mapping images of a single PdAg and $PdAg_3$ nanoparticle c) PdAg/CNT, d) $PdAg_3$/CNT.

to observe a change in the catalysts' oxidation states (Fig. S1). The results showed no apparent change in the surface oxidation states of the catalysts, reflecting good stability of the catalysts. It is worth mentioning that wide XPS spectra of as-prepared catalysts after a 2 h reaction revealed the additional presence of F and Cl elements among Pd, Ag, C, and O elements that originated as impurities either from the potassium hydroxide electrolyte or from the anion-exchange membrane used in the reaction (Fig. S2).

HAADF-STEM elemental mapping images are shown in Fig. 2c and d, revealing a homogeneous distribution of Pd and Ag in a single PdAg and $PdAg_3$ nanoparticle along with well-developed crystalline structure; this further displays the alloy feature of PdAg/CNT and $PdAg_3$/CNT. The aqueous-phase reduction method achieved very small Pd nanoparticles under these synthesis conditions, while nanoparticles containing Ag were slightly larger and more highly developed, as can be seen in the HAADF-STEM images. While it is interesting to find that nanoparticles are not exactly round-shaped, this may be due to the synthesis conditions, and details of PdAg nanoparticle growth should be further investigated in our future work.

3.2. Electrocatalytic oxidation of glycerol study of Pd/CNT, PdAg/CNT, $PdAg_3$/CNT, and Ag/CNT in half-cell

CV profiles were conducted to study electrocatalytic oxidation of glycerol over Pd/CNT, PdAg/CNT, $PdAg_3$/CNT, and Ag/CNT catalysts, as shown in Fig. 3. The results show that Pd and Ag alloyed together exhibited higher current density and lower onset potential than monometallic Pd/CNT and Ag/CNT catalysts. The onset poten-

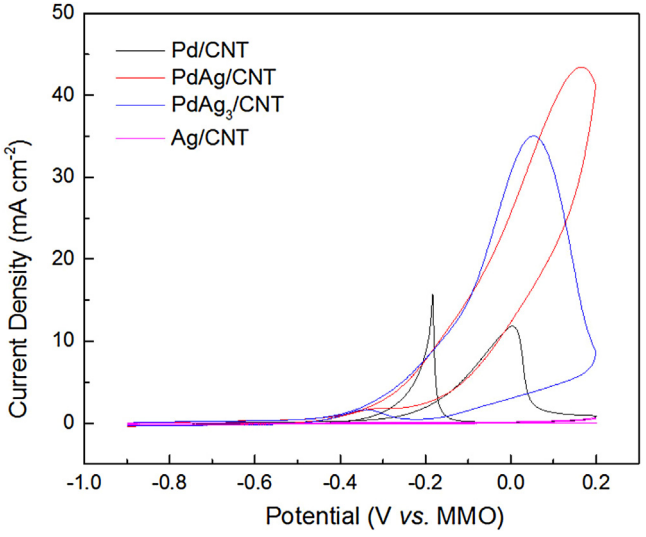

Fig. 3. Cyclic Voltammograms of glycerol oxidation reaction on Pd/CNT, PdAg/CNT, $PdAg_3$/CNT, and Ag/CNT catalysts in 1.0 M KOH + 0.1 M glycerol, 50 mV s^{-1}, 25 °C.

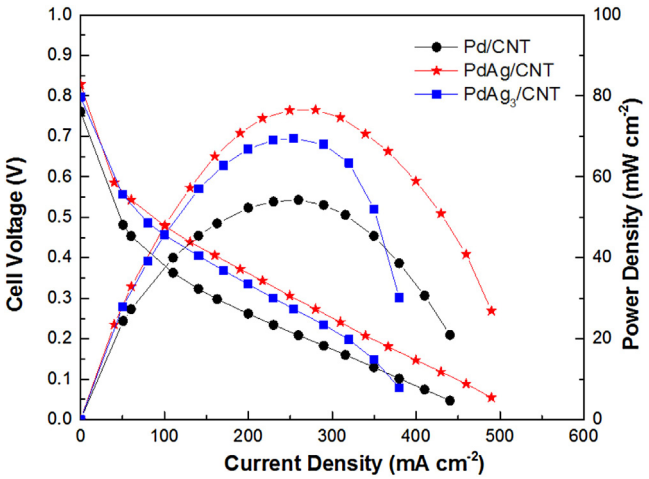

Fig. 4. Polarization and power density curves of direct glycerol AEMFC with different anode catalysts (Pd/CNT, 0.5 mg cm^{-2}; PdAg/CNT, 1.0 mg cm^{-2}; $PdAg_3$/CNT, 2.0 mg cm^{-2}). AEM: Tokuyama A201; cathode catalyst: Fe-based catalyst (Acta 4020), 3.0 mg cm-2; anode fuel: 2.0 M KOH + 1.0 M glycerol, 2.0 mL min^{-1}, cathode fuel: O_2, 200 sccm, ambient pressure, 60 °C.

tial of glycerol oxidation shifted more negatively with increasing Ag content −0.44 V > −0.39 V > −0.35 V for $PdAg_3$/CNT, PdAg/CNT, and Pd/CNT, but the current density for PdAg/CNT is higher than that for $PdAg_3$/CNT, indicating that further addition of Ag will diminish the current density due to blockage of Pd active sites by the additional Ag content, so the synergetic effect of PdAg/CNT improves the total reaction rate of the glycerol oxidation reaction. The Ag/CNT catalyst, however, displayed very little or no activity directed toward electrocatalytic glycerol oxidation at the same applied potential. In general, it can be concluded that Ag is relatively catalytically inactive towards alcohol oxidation within the fuel cell anode potential window (<−0.2 V vs. MMO).

3.3. Electrocatalytic oxidation of glycerol study of Pd/CNT, PdAg/CNT, and $PdAg_3$/CNT in single-cell

Cell polarization and power density curves of direct glycerol AEMFC using Pd/CNT, PdAg/CNT, and $PdAg_3$/CNT anode catalysts are shown in Fig. 4. The open circuit voltage (OCV) of the direct glycerol AEMFC with PdAg/CNT was 0.83 V, 0.03 V higher than that for $PdAg_3$/CNT and 0.07 V higher than that for Pd/CNT. The peak power density (PPD) of the direct glycerol AEMFC with PdAg/CNT was 76.5 mW cm^{-2}, 9.1% higher than that for $PdAg_3$/CNT and 29.0% higher than that for Pd/CNT. It is also interesting to observe that $PdAg_3$/CNT achieves a limited reaction rate in the higher current density region because of reactant mass transfer issues. The higher content of Ag causes the more active sites of the Pd catalyst to be covered by the Ag, leading to a decrease in performance. These single-cell performance results are consistent with half-cell results.

3.4. Glycerol oxidation product distribution in AEMFCs on Pd/CNT, PdAg/CNT, and $PdAg_3$/CNT

We further examined glycerol oxidation products from using Pd/CNT, PdAg/CNT, and $PdAg_3$/CNT anode catalysts for 2 h at 60 °C in AEM-DGFC at constant fuel cell voltage (0.1 V). The oxidation products were analyzed using HPLC. Table 2 shows the product selectivity distribution of glycerol oxidation for Pd/CNT, PdAg/CNT, and $PdAg_3$/CNT. It can be observed that the selectivity of C_2 species, i.e., oxalate and glycolate on Pd/CNT, PdAg/CNT, and $PdAg_3$/CNT, increased as the Ag content increased, indicating that Ag contributed to a deeper C—C bond cleavage. Conversely,

Table 2
Product selectivity distribution of electrocatalytic oxidation of glycerol on Pd/CNT, PdAg/CNT, and $PdAg_3$/CNT in AEM-DGFC. Anode fuel: 4.0 M KOH + 1.0 M glycerol, 2.0 mL min^{-1}, cathode fuel: O_2, 200 sccm, ambient pressure, 60 °C. The below numbers are in%.

	Oxalate	Glycolate	Tartronate	Mesoxalate	Glycerate	Lactate
	12e$^-$	8e$^-$	8e$^-$	10e$^-$	4e$^-$	2e$^-$
Pd/CNT	25.3	8.5	39.5	3.8	21.7	1.2
PdAg/CNT	35.9	20.9	26.4	1.5	14.2	1.1
$PdAg_3$/CNT	39.2	37.9	13.7	0	8.8	0.3

all the C_3 species, i.e., tartronate, mesoxalate, glycerate, and lactate on Pd/CNT, PdAg/CNT, $PdAg_3$/CNT, decreased as the Ag content increased. The corresponding conversion of glycerol is 48.4%, 55.0%, and 43.0% for Pd/CNT, PdAg/CNT, and $PdAg_3$/CNT, respectively. The increase in Ag content has resulted in higher faraday efficiencies of 58.2% for Pd/CNT, 63.1% for PdAg/CNT, and 65.7% for $PdAg_3$/CNT, while the fuel utilization efficiency exhibits a volcano trend as shown in Table 3 because since the fuel utilization efficiency has a relationship with the conversion (Fuel utilization efficiency = faradaic efficiency × conversion), a higher Ag content may block the active sites of Pd and result in a decrease in the conversion of $PdAg_3$/CNT, leading to the fuel utilization efficiency drop. It is also very interesting to observe that PdAg not only improves the faradaic efficiency by 8.4% (from 58.2% to 63.1%), but also enhances the peak power density by 29% (from 59.3 to 76.5 mW/cm^2).

In our previous work, we reported a high pH alkaline environment (6.0 M KOH+ 1.0 M glycerol), targeting a high glycerol electro-oxidation rate [51]. In the present work, we reduced the alkaline concentration from 6.0 to 4.0 M and then 2.0 M, based on considerations of environmental impact and fuel cell device material compatibility. As the KOH concentration increased from 2.0 M to 4.0 M, the glycerol conversion on PdAg/CNT jumped from 50.4% to 55.0% due to the promoted deprotonation of glycerol in a higher pH environment (Table 3 and Table S1). A higher KOH concentration also facilitates the oxidation of hydroxyl groups in glycerol, leading to higher selectivity of C_3 products, as shown in our previous study [51]. It can be noted that varying the KOH concentration (from 6.0 M to 2.0 M) has only minor effects on product distribution.

3.5. Electrocatalytic oxidation of products and intermediates of glycerol in half-cell

To further investigate the electrocatalytic oxidation of glycerate, mesoxalate, tartronate, lactate, oxalate, and glycolate over Pd/CNT, PdAg/CNT, $PdAg_3$/CNT, and Ag/CNT catalysts, CVs were conducted at 60°C, with the results shown in Fig. 5. The activities of the prepared catalysts for oxidation of intermediates were compared in a half-cell reactor by observing the oxidation onset potential and peak current density. The onset of glycerate oxidation (Fig. 5a), containing two alcohols and one carboxylic acid groups, occurred at a much lower potential (-0.47 V) on PdAg/CNT compared to that for Pd/CNT and Ag/CNT, reflecting the synergistic effect of Pd-Ag in promoting the alcohol group oxidation. Similarly, in the low potential range, the current density for PdAg/CNT was significantly higher than that for Pd/CNT and Ag/CNT catalysts within the fuel cell anode potential (−0.22 V vs. MMO). This is consistent with electro-oxidation glycolate (containing one primary alcohol and one carboxylic acid group, Fig. 5f) results, for which PdAg shows the lowest potential (−0.56 V). In comparison, oxalate containing two carboxylic acid groups is inactive over all four catalysts (Fig. 5e), indicating that it is a dead-end chemical because a carboxylic acid group cannot be further oxidized. It is interesting to note that tartronate and lactate are quite stable under the scanned potential range over the four catalysts (Fig. 5c and d),

Table 3
Conversion, carbon balance, average electron transfer, faraday efficiency, and fuel utilizations of electrocatalytic oxidation of glycerol on Pd/CNT, PdAg/CNT, and $PdAg_3$/CNT in AEM. Anode fuel: 4.0 M KOH + 1.0 M glycerol, 2.0 mL min^{-1}, cathode fuel: O_2, 200 sccm, ambient pressure, 60 °C.

	Conversion (%)	Carbon Balance (%)	Average Electron Transfer	Faraday Efficiency (%)	Fuel Utilization (%)	Power Density (mW cm^{-2})
Pd/CNT	48.4	94.2	8.1	58.2	28.2	54.3
PdAg/CNT	55.0	89.9	8.8	63.1	34.7	76.5
$PdAg_3$/CNT	43.0	82.1	9.1	65.7	28.3	69.2

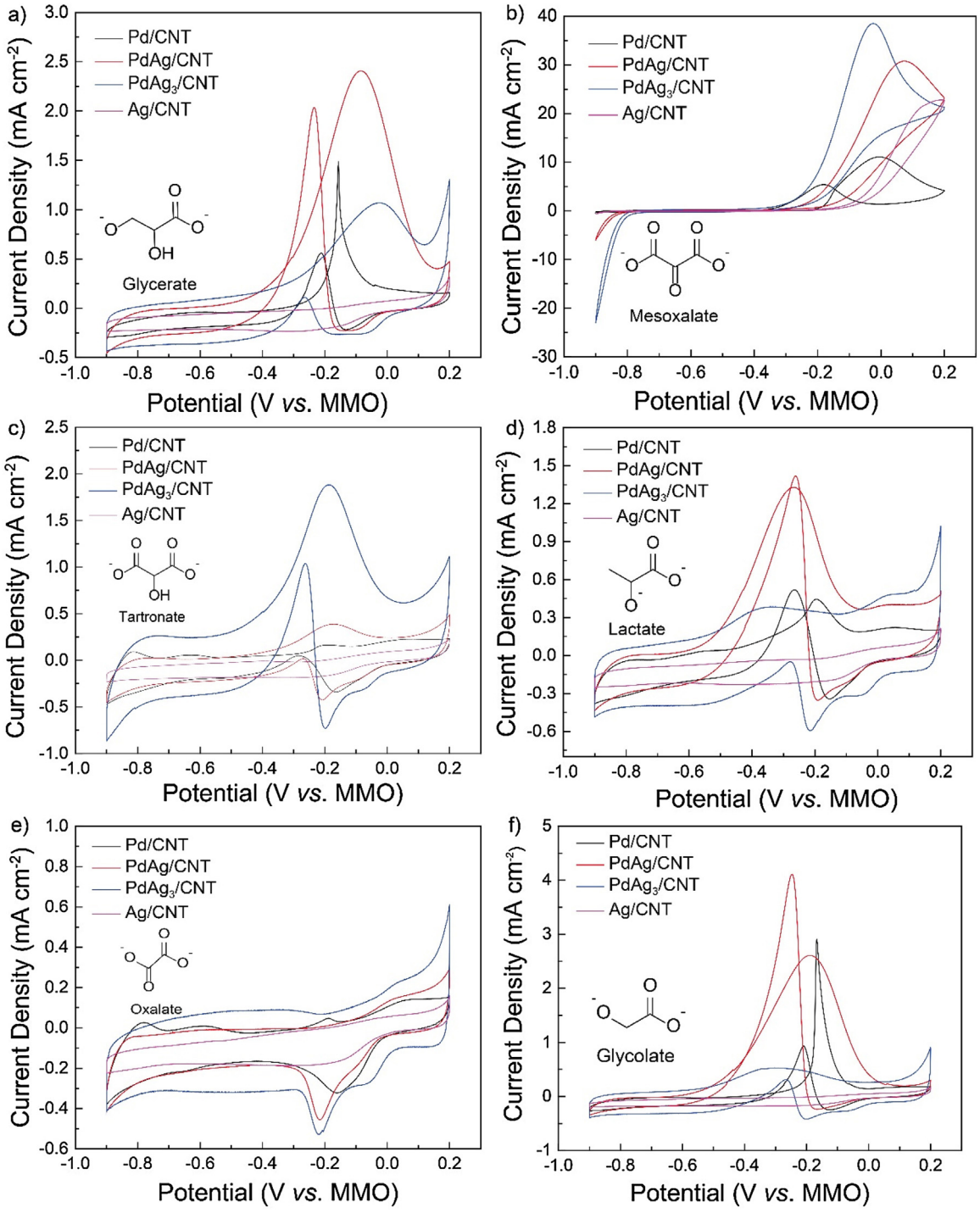

Fig. 5. Cyclic Voltammograms of Pd/CNT, PdAg/CNT, $PdAg_3$/CNT, and Ag/CNT for glycerol oxidation products and intermediates in 1.0 M KOH + 0.1 M (a) glycerate, (b) mesoxalate, (c) tartronate, (d) lactate, (e) oxalate, and (f) glycolate at 50 mV s^{-1}, 60 °C.

even though they both contain an alcohol group; this might be due to a steric effect in which the alcohol group is protected by two adjacent inert carboxylic groups or methyl group. Mesoxalate is relatively stable on a Ag catalyst without generating notable current density at <−0.22 V (Fig. 5b) in comparison to other Pd-containing catalysts, because further oxidation of C_3 mesoxalate will result in C—C bond cleavage; this result suggests that Ag itself does not facilitate C—C cleavage. We must clarify that Ag itself does not effectively facilitate C—C cleavage of desorbed mesoxalate to C_2 species as much as Pd does, especially within the AEM-DAFC anode potential window (< 0.7 V vs. RHE). However, since Ag's specific activity (0.208 mA/cm$^2_{Ag}$) towards mesoxalate is 5.5 times that of Pd (0.038 mA/cm$^2_{Pd}$) at 0.7 V vs. RHE, Ag will remarkably help PdAg/CNT to break C—C bond of mesoxalate when its particle size reduces to 2.3 nm. The higher Ag atomic ratio in the catalyst, along with the higher activity of the catalyst towards mesoxalate oxidation, produces more C—C cleavage of mesoxalate to C_2 and C_1 products. We further found that desorbed tartronate as an oxidation of intermediates in the bulk electrolyte is quite stable for all catalysts, PdAg/CNT slightly outperforms Pd/CNT with respect to current density, as shown in Fig. 5c. However, it is interesting to note that tartronate is more active on $PdAg_3$/CNT catalysts at the higher temperature of 60°C, compared to its activity at 25°C (Fig. S3); the mechanism should be further studied. For glycolate oxidation (Fig. 5f), PdAg/CNT exhibits the best activity compared to the other three catalysts (Pd/CNT, Ag/CNT, and Pd_1Ag_3/CNT), and also a close onset potential but lower current density compared to glycerate oxidation. Ag shows virtually no activity for glycolate oxidation and this interesting result supports our hypothesis that adjacent inert groups (methyl or carboxylic acid) could protect an alcohol group from oxidation. Glycerate has two alcohol groups: one primary, one secondary adjacent to a carboxylic group, while glycolate has one primary alcohol group, tartronate has one middle alcohol group adjacent to two carboxylic groups, and lactate has one middle alcohol group adjacent to a methyl and a carboxylic group, so the generated current density exactly follows the trend: glycerate > glycolate > tartronate ≈ lactate.

The electrocatalytic oxidation of intermediates of glycerol over the four catalysts were further investigated by CVs at 25°C. As shown in Fig. S3, the onset potentials for these four catalysts moved to slightly more positive positions as the working temperature decreased to 25°C, while the current density decreased for all these catalysts across the whole applied potential range. These shifts in onset potential and peak current density, indicate that at lower temperature (25°C) kinetics are slower for electrooxidation of glycerol intermediates on four catalysts.

To test performance of electrocatalytic activity of glycerol oxidation intermediates over PdAg/CNT in AEMFCs, all the intermediates (glycerate, tartronate, mesoxalate, lactate, glycolate, and oxalate) were fed as anode fuel. It was observed that glycerate and mesoxalate were the only two intermediates showing stable performance under the fuel cell test conditions. Tartronate, lactate, and the other C_2 intermediates glycolate and oxalate showed no current generated to produce power in AEMFCs. The DGFC with mesoxalate showed a high peak power density of 15 mW/cm^2, while the one with glycerate produced a value of 9 mW/cm^2. The trend in intermediates' oxidation activity obtained from the single fuel cell (peak power density) is fully consistent with half-cell tests (current density), as shown in Figs. 5 and 6: mesoxalate (15 mA/cm^2, 15 mW/cm^2) > glycerate (1.75 mA/cm^2, 9 mW/cm^2) > glycolate (0.7 mA/cm^2, unstable fuel cell performance) > tartronate ≈ lactate (hardly any current generated in both half-cell and single cell).

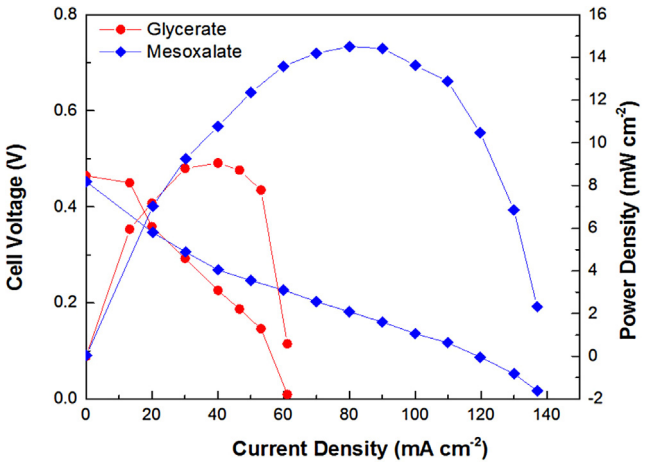

Fig. 6. Polarization and power density curves of direct glycerol oxidation products (C_3) with PdAg/CNT anode catalyst at optimized operating conditions. AEM: Tokuyama A901; cathode catalyst: Fe-based catalyst (Acta 4020), 3.0 mg cm^{-2}; anode fuel: 2.0 M KOH + 0.3 M fuel (mesoxalate, glycerate).

3.6. Electrocatalytic oxidation of mesoxalate and glycerate product intermediates of glycerol in single-cell

Electrocatalytic oxidation of mesoxalate and glycerate (product intermediates of glycerol oxidation) was further examined to elucidate the overall glycerol oxidation pathway by continuously looping 4.0 M KOH + 0.5 M mesoxalate or glycerate (20 mL) from a plastic vessel into the anode compartment of an AEMFC for 2 h at a constant fuel-cell voltage of 0.1 V on PdAg/CNT anode catalyst at 60 °C. At lower fuel-cell voltage (0.1 V) glycerol oxidation conversion would be expected to react faster [19]. Oxalate and formate products were detected with selectivities of 91.8% and 8.2% at 78.7% conversion of mesoxalate. Tartronate and oxalate were detected with selectivities of 53.0% and 47.0% at 91.3% conversion of glycerate. It can be seen that oxidation of C_3 product intermediates (mesoxalate and tartronate) of glycerol provides deeper oxidation and C—C bond cleavage to C_2 species, i.e., oxalate.

3.7. Proposed reaction pathway for glycerol oxidation over PdAg/CNT

Based on the obtained half-cell and single cell activity and product distribution results, Fig. 7 illustrates our proposed reaction pathways for the oxidation of glycerol with main C_3 and C_2 oxidation products over PdAg/CNT in AEM-DGFC. The first step was to oxidize one primary hydroxyl group in glycerol to generate glycerate, making glycerate a stable reaction intermediate during the glycerol oxidation reaction. Glycerate was furthermore rapidly oxidized into C_3 tartronate and C_2 oxalate (a C—C cleavage product) with selectivities of 53.0% and 47.0%, respectively. This step was confirmed using electrocatalytic oxidation of glycerate in AEM-DGFC. The alcohol group of tartronate is surrounded by two carboxylic acid groups, so it is reasonable to hypothesize that mesoxalate is produced through the direct oxidation of the hydroxyl group in tartronate (or a relevant C_3reactive intermediate) at a slow rate, with Pd the active site rather than Ag (3.8% on Pd, 1.5% on PdAg, and 0 on $PdAg_3$, see Table. 2). Electrocatalytic oxidation of mesoxalate in AEM-DGFC confirmed the cleavage of C—C bond of mesoxalate to oxalate and formate as products in AEM-DGFC; this is another route to production of C_2 oxalate. Oxalate containing two carboxylic acid groups is inactive over all four catalysts (per half-cell results), indicating that it is also a dead-end

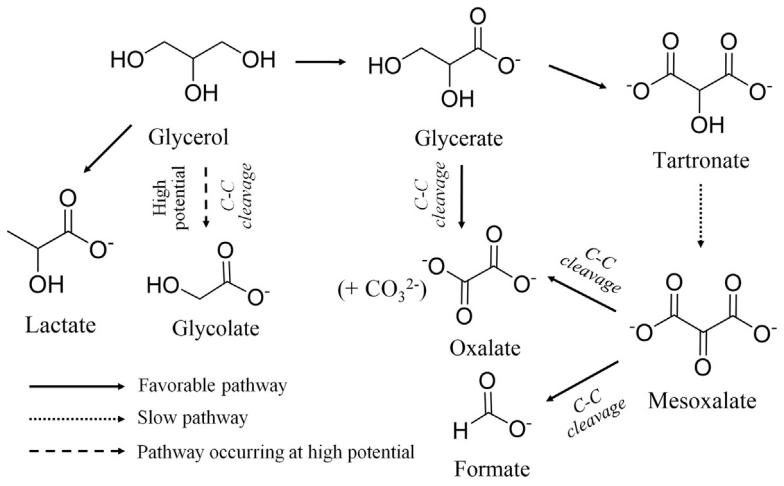

Fig. 7. Proposed reaction pathway for oxidation of glycerol on PdAg/CNT in alkaline media. *Note: these reaction pathways do not necessarily indicate elementary reaction steps.*

chemical because a carboxylic acid group cannot be further oxidized, in good agreement with previous observations. The glycolate from the direct C—C bond cleavage of glycerol in the oxidation process was not detected over PdAg catalysts at this low applied cell voltage. Our previous work showed that glycolate can be formed from the adsorbed glycerate and even desorbed tartronate via C—C cleavage on Au catalyst, but this requires higher applied potentials (>0.9 V vs. RHE) [19,53], further suggesting that the reaction pathways and product distributions are strongly potential dependent. We hypothesize that lactate in small amount (<2%, Table. 2) is generated through a coupled homogeneous transformation of some C_3 intermediates (likely glyceraldehyde) in alkaline electrolyte; indeed, distinguishing the pathways of electrochemical oxidation and electrocatalytic oxidation is an interesting research topic on which we are currently working.

4. Conclusions

Carbon nanotube (CNT) supported Pd, PdAg, $PdAg_3$, and Ag nanoparticles with small sizes (2.0 nm for Pd/CNT, 2.3 nm for PdAg/CNT, 2.4 nm for $PdAg_3$/CNT, and 13.9 nm for Ag/CNT) and narrow size distributions were synthesized through a modified aqueous-phase reduction method and served as working catalysts. XPS spectra show that by alloying with Ag, more metallic state Pd is presented on the surface. The higher performance of AEM-DGFC with PdAg anode catalyst compared to that with Pd/CNT anode catalyst suggests that PdAg can improve the glycerol reaction rate (kinetics). The oxidation product analysis demonstrates the selectivity of the C_2 species, i.e., oxalate and glycolate on Pd/CNT, PdAg/CNT, and $PdAg_3$/CNT increased as the Ag content increased, indicating that Ag contributed to deeper oxidation and C—C bond cleavage. Therefore, by employing bimetallic PdAg/CNT along with optimizing reaction conditions, high overall AEM-DGFC performances (in terms of both electrical power density and fuel utilization efficiency) can be achieved. Electrocatalytic oxidation of glycerol and intermediates in an AEM-DGFC with product analysis, along with CVs of oxidation intermediates, was conducted to elucidate the electrocatalytic oxidation pathways on PdAg catalyst. We find that glycerate and mesoxalate are the two C_3 intermediates leading to C—C cleavage product of oxalate, while tartronate is a relatively inert chemical whose slow further oxidation generates mesoxalate, lactate is possibly produced from homogeneous transformation of C_3 intermediates, and glycolate is not a favorable product under lower fuel cell anode potentials. The enhancement of glycerol oxidation over PdAg bimetallic catalyst is proposed to occur through a synergistic effect of Ag's promotion of intermediate aldehyde oxidation and C—C breakage of C_3 oxygenates along with a larger amount of Pd^0 presented on the PdAg nanoparticle surface (determined by ex-situ XPS), as supported by combining physical characterization, electrochemical activity tests and product analysis of relevant glycerol intermediates oxidation.

Acknowledgements

We acknowledge financial support from the US National Science Foundation (CBET-1501124 and 1159448), the Iowa State University startup fund, the Ames Lab startup fund and an Iowa Energy Center (IEC) Opportunity Grant. We thank Dr. Dapeng Jing of Material Analysis and Research Laboratory of ISU for XPS analysis and also Zhiyuan Qi of Chemistry Department for ICP-MS analysis. The authors are grateful to Ryan F. McSweeney and Baitong Chen of Iowa State University for assistance in fuel cell experiments. W. Li is grateful to the support of his Richard Seagrave Professorship.

References

[1] D. Helm, Oxford Rev. Econ. Policy 32 (2016) 191–205.
[2] T.P. Vispute, H. Zhang, A. Sanna, R. Xiao, G.W. Huber, Science 330 (2010) 1222–1227.
[3] B. Richter, D. Goldston, G. Crabtree, L. Glicksman, D. Goldstein, D. Greene, D. Kammen, M. Levine, M. Lubell, M. Savitz, D. Sperling, F. Schlachter, J. Scofield, J. Dawson, Rev. Mod. Phys. 80 (2008) S1–S109.
[4] N. Benipal, J. Qi, J.C. Gentile, W. Li, Renew. Energ. 105 (2017) 647–655.
[5] J.V. Gerpen, Fuel Process. Technol. 86 (2005) 1097–1107.
[6] C.-H. Zhou, J.N. Beltramini, Y.-X. Fan, G.Q. Lu, Chem. Soc. Rev. 37 (2008) 527–549.
[7] C.L. Bianchi, P. Canton, N. Dimitratos, F. Porta, L. Prati, Catal. Today 102–103 (2005) 203–212.
[8] B. Katryniok, H. Kimura, E. Skrzynska, J.-S. Girardon, P. Fongarland, M. Capron, R. Ducoulombier, N. Mimura, S. Paul, F. Dumeignil, Green Chem. 13 (2011) 1960–1979.
[9] M. Pagliaro, R. Ciriminna, H. Kimura, M. Rossi, C. Della Pina, Angew. Chem. Int. Ed. 46 (2007) 4434–4440.
[10] L. Thia, M. Xie, Z. Liu, X. Ge, Y. Lu, W.E. Fong, X. Wang, ChemCatChem 8 (2016) 3272–3278.
[11] C.H. Zhou, J.N. Beltramini, Y.X. Fan, G.Q. Lu, Chem. Soc. Rev. 37 (2008) 527–549.
[12] S. Carrettin, P. McMorn, P. Johnston, K. Griffin, C.J. Kiely, G.J. Hutchings, Phys. Chem. Chem. Phys. 5 (2003) 1329–1336.
[13] R. Bauer, D. Hekmat, Biotechnol. Prog. 22 (2006) 278–284.
[14] C.K. Dyer, Fuel Cells Bull. 2002 (2002) 8–9.
[15] S.K. Kamarudin, F. Achmad, W.R.W. Daud, Int. J. Hydrogen Energy 34 (2009) 6902–6916.
[16] M. Winter, R.J. Brodd, Chem. Rev. 104 (2004) 4245–4270.
[17] E.H. Yu, U. Krewer, K. Scott, Energies 3 (2010) 1499.
[18] E. Antolini, E.R. Gonzalez, J. Power Sources 195 (2010) 3431–3450.
[19] L. Xin, Z. Zhang, Z. Wang, W. Li, ChemCatChem 4 (2012) 1105–1114.
[20] Z. Zhang, L. Xin, K. Sun, W. Li, Int. J. Hydrogen Energy 36 (2011) 12686–12697.
[21] R.L. Arechederra, B.L. Treu, S.D. Minteer, J. Power Sources 173 (2007) 156–161.

[22] A.S. Aricò, V. Baglio, V. Antonucci, Wiley-VCH Verlag GmbH & Co. KGaA2009, pp. 1–78.
[23] J.S. Spendelow, A. Wieckowski, Phys. Chem. Chem. Phys. 9 (2007) 2654–2675.
[24] F.T. Wagner, B. Lakshmanan, M.F. Mathias, J. Phys. Chem Lett. 1 (2010) 2204–2219.
[25] J. Qi, L. Xin, Z. Zhang, K. Sun, H. He, F. Wang, D. Chadderdon, Y. Qiu, C. Liang, W. Li, Green Chem. 15 (2013) 1133–1137.
[26] M.L. Faro, M. Minutoli, G. Monforte, V. Antonucci, A.S. Aricò, Biomass Bioenergy 35 (2011) 1075–1084.
[27] G.S. Prakash, F.C. Krause, F.A. Viva, S. Narayanan, G.A. Olah, J. Power Sources 196 (2011) 7967–7972.
[28] A. Arico, P. Creti, E. Modica, G. Monforte, V. Baglio, V. Antonucci, Electrochim. Acta 45 (2000) 4319–4328.
[29] S.A.Kuliyev, Mahmud.Mat, B. Ibrahimoglu, Mustafa D.Kozlu, ECS Transactionienna, Austria Solid Oxide Fuel Cells 11(SOFC-XI), 2009, pp. 216th ECS Meeting.
[30] J.B. Xu, T.S. Zhao, Y.S. Li, W.W. Yang, Int. J. Hydrogen Energy 35 (2010) 9693–9700.
[31] L. Jiang, G. Sun, S. Sun, J. Liu, S. Tang, H. Li, B. Zhou, Q. Xin, Electrochim. Acta 50 (2005) 5384–5389.
[32] S. Song, P. Tsiakaras, Appl. Catal. B: Environ. 63 (2006) 187–193.
[33] A.C. Garcia, M.J. Kolb, C. van Nierop y Sanchez, J. Vos, Y.Y. Birdja, Y. Kwon, G. Tremiliosi-Filho, M.T.M. Koper, ACS Catal. 6 (2016) 4491–4500.
[34] L. Ma, D. Chu, R. Chen, Int. J. Hydrogen Energy 37 (2012) 11185–11194.
[35] H. Wang, C. Xu, F. Cheng, M. Zhang, S. Wang, S.P. Jiang, Electrochem. Commun. 10 (2008) 1575–1578.
[36] W.J. Zhou, W.Z. Li, S.Q. Song, Z.H. Zhou, L.H. Jiang, G.Q. Sun, Q. Xin, K. Poulianitis, S. Kontou, P. Tsiakaras, J. Power Sources 131 (2004) 217–223.
[37] W.J. Zhou, S.Q. Song, W.Z. Li, G.Q. Sun, Q. Xin, S. Kontou, K. Poulianitis, P. Tsiakaras, Solid State Ionics 175 (2004) 797–803.
[38] M. Sankar, N. Dimitratos, D.W. Knight, A.F. Carley, R. Tiruvalam, C.J. Kiely, D. Thomas, G.J. Hutchings, ChemSusChem 2 (2009) 1145–1151.
[39] N. Dimitratos, F. Porta, L. Prati, Appl. Catal. A: Gen. 291 (2005) 210–214.
[40] P. Gallezot, Catal. Today 37 (1997) 405–418.
[41] R. Garcia, M. Besson, P. Gallezot, Appl. Catal. A: Gen. 127 (1995) 165–176.
[42] W. Li, J. Chen, C. Yan, X. Hao, J. Alloys Compd. 632 (2015) 178–184.
[43] G.Z. Hu, F. Nitze, X. Jia, T. Sharifi, H.R. Barzegar, E. Gracia-Espino, T. Wagberg, RSC Adv. 4 (2014) 676–682.
[44] J. Zhao, M. Shao, D. Yan, S. Zhang, Z. Lu, Z. Li, X. Cao, B. Wang, M. Wei, D.G. Evans, X. Duan, J. Mater. Chem. A 1 (2013) 5840–5846.
[45] L. Zhang, H. Wang, X. Li, F. Xia, Y. Liu, X. Xu, J. Gao, F. Xing, Electrochim. Acta 172 (2015) 42–51.
[46] H. Rostami, A.A. Rostami, A. Omrani, Int. J. Hydrogen Energy 40 (2015) 10596–10604.
[47] E.J. Lim, Y. Kim, S.M. Choi, S. Lee, Y. Noh, W.B. Kim, J. Mater. Chem. A 3 (2015) 5491–5500.
[48] L. Li, M. Chen, G. Huang, N. Yang, L. Zhang, H. Wang, Y. Liu, W. Wang, J. Gao, J. Power Sources 263 (2014) 13–21.
[49] J. Cai, Y. Huang, Y. Guo, Int. J. Hydrogen Energy 39 (2014) 18256–18263.
[50] Z. Zhang, C. Zhang, J. Sun, T. Kou, C. Zhao, RSC Adv. 2 (2012) 11820–11828.
[51] J. Qi, N. Benipal, C. Liang, W. Li, Appl. Catal. B: Environ. 199 (2016) 494–503.
[52] N. Benipal, J. Qi, P.A. Johnston, J.C. Gentile, R.C. Brown, W. Li, Fuel 185 (2016) 85–93.
[53] J. Qi, L. Xin, D.J. Chadderdon, Y. Qiu, Y. Jiang, N. Benipal, C. Liang, W. Li, Appl. Catal. B: Environ. 154–155 (2014) 360–368.
[54] W. Li, M. Waje, Z. Chen, P. Larsen, Y. Yan, Carbon 48 (2010) 995–1003.
[55] Z. Zhang, L. Xin, J. Qi, D.J. Chadderdon, W. Li, Appl. Catal. B: Environ. 136–137 (2013) 29–39.